

Maximum performance of strange-jet tagging at hadron colliders

Johannes Erdmann, Olaf Nackenhorst and Sonja Verena Zeißner¹

Lehrstuhl für Experimentelle Physik IV, TU Dortmund, Otto-Hahn-Straße 4a, 44227 Dortmund, Germany

E-mail: sonja.zeissner@tu-dortmund.de

ABSTRACT: The maximum achievable performance of strange-jet tagging at hadron colliders and the loss in performance in different detector designs is estimated based on simulated truth jets from strange-quark and down-quark hadronisation. Both jet types are classified with a recurrent neural network using long short-term memory units, at first assuming an ideal detector and then detector layouts with different combinations of ideal tracking detectors, Cherenkov detectors, and calorimeters. A comparison between the different detector layouts is made in order to study the strengths of these detector types for strange-jet tagging. The different scenarios are compared to the separation power from strange-hadron decays to two charged particles as a benchmark, such as $K_S \rightarrow \pi^+ \pi^-$.

KEYWORDS: Analysis and statistical methods; Data processing methods; Particle identification methods

¹Corresponding author

Contents

1	Introduction	1
2	Simulated samples	2
3	Detector scenarios	5
3.1	Ideal detectors	5
3.1.1	Universal collider detector	5
3.1.2	Universal collider detector excluding the beampipe	7
3.1.3	Infinite and finite tracking detectors	7
3.1.4	Cherenkov tracking detector	7
3.1.5	Calorimeters with and without separation into electromagnetic and hadronic components	8
3.2	Strange-hadron decays to two charged particles	9
4	Neural-network architecture	9
5	Results	11
5.1	Universal collider detectors	11
5.2	Tracking and Cherenkov detectors	12
5.3	Calorimeters	14
5.4	Strange-hadron decays to two charged particles	15
6	Conclusions	16

1 Introduction

The identification of the flavour of a jet, i.e. the type of elementary particle from which the jet originated, is a crucial experimental technique at collider experiments, such as experiments at the Large Hadron Collider. The identification of jets that originate from b -quarks [1] is an established technique at the ATLAS [2] and CMS [3] experiments with a multitude of applications. Methods for the identification of jets from c -quarks [3, 4] and gluons [5–17] have also been developed in recent years, as well as the identification of jets with large radius parameters that stem from hadronic decays of top quarks [18–26], W and Z bosons [21, 25, 27–33], and Higgs bosons [25, 33–37].

Algorithms for the identification of jets from strange-quarks (s -jets) are currently not in use at the Large Hadron Collider. Such a strange-tagging (or s -tagging) algorithm, however, would complement the existing algorithms for the identification of the jet flavour and could open new opportunities in the analysis of the data, such as searches for the decays $t \rightarrow W^+ s$ [38] and $H \rightarrow s\bar{s}$ [39]. As s -jets can be distinguished from jets that stem from b - and c -quarks with b - and

c -tagging algorithms, the main challenge of an s -tagging algorithm is the separation from jets that stem from u - and d -quarks. At the Large Electron-Positron Collider, Cherenkov detectors were used to identify s -jets [40, 41], exploiting their identification power for charged kaons. More recently, machine-learning methods have been explored for s -tagging based on tracking [42] and additional calorimeter information [43]. However, these studies show that it is challenging to achieve a good separation of s - and d -/ u -jets — in particular compared to the excellent separation that is achieved for b - and c -taggers. One reason is that strange-hadrons, such as kaons and Λ baryons, do not only appear in the fragmentation of s -quarks but also are frequently part of d - and u -jets. Another reason is that the unique identification of these strange-hadrons is experimentally challenging: (1) K_S mesons and Λ baryons often decay within the inner tracking detectors of collider experiments, but their unambiguous identification is mainly possible if they decay to two charged particles and the tracks of both decay products are well-measured; (2) K_L and K^\pm mesons have long lifetimes and mostly do not decay before producing hadronic showers in the calorimeters, which are then difficult to distinguish from the showers of other hadrons; (3) tracks from K^\pm mesons could, in principle, be distinguished from other charged particles with the use of Cherenkov detectors or dE/dx measurements, but these are also limited in precision.

The goal of this paper is to separate the fragmentation and experimental effects on s -tagging. Assuming an ideal detector that could measure all particles in an s -jet perfectly, the maximum performance of an s -tagger solely based on the differences in the fragmentations of s - and d -jets is determined. While this clearly cannot be achieved in a realistic experiment, it defines a useful benchmark and an upper bound for more realistic s -tagging optimizations. In order to determine this benchmark, neural networks are trained based on Monte-Carlo simulations in order to separate s - and d -jets using the properties of their constituent particles¹. The application of machine learning in high-energy physics has proven to be a successful approach, especially for the classification of jets [2–4, 8–17, 19–26, 28, 31–34, 36, 37, 42–53]. Here, long short-term memory recurrent neural networks [54] are used, which provide a complex model to capture differences in the jet-constituent properties.

In addition, several scenarios with different combinations of idealized detector components are studied. These provide an estimate of the maximum performance that can be achieved for s -tagging based on tracking information, additional Cherenkov detectors, and with calorimeter information. These studies provide guidance for further developments for s -jet tagging based on these detector components.

2 Simulated samples

To compare jets originating from s - and d -quarks, di-quark production events in proton–proton collisions, i.e. $pp \rightarrow s\bar{s}$ and $pp \rightarrow d\bar{d}$, are simulated at $\sqrt{s} = 13$ TeV. The matrix element is simulated at leading order in α_S with MadGraph_aMC@NLO version 2.6.7 [55] using the NNPDF2.3LO set of parton distribution functions [56]. The parton shower and hadronisation is simulated with Pythia 8.2.35 [57]. The events are not passed through any detector simulation, hence it is assumed that all quantities are measured perfectly. All resulting particles with a non-zero

¹The s -tagging performance for a tagger based on tracking information was found to be similar for d - and u -jets [42], so that we limit ourselves in this study to d -jets as only one background class.

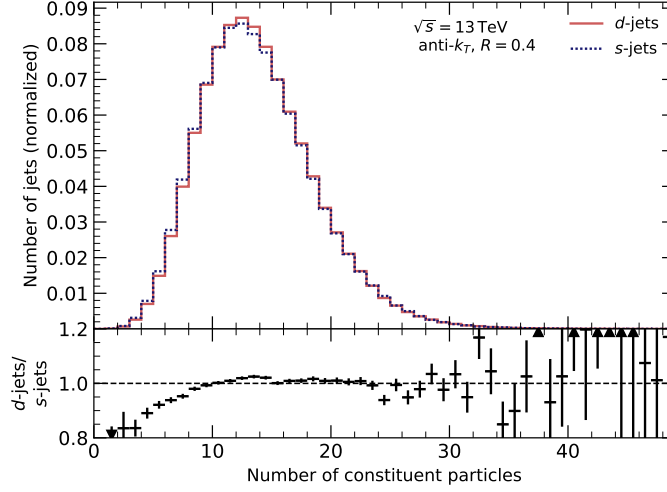


Figure 1. Distribution of the number of constituent particles per s - and d -jet clustered from all particles with a lifetime greater zero.

lifetime are clustered into jets with the anti- k_T -algorithm [58] with a radius parameter of $R = 0.4$ using FastJet [59]. In order to label the flavour of the jets, the s - and d -quarks from the matrix element are ghost-matched [60] to the resulting jets.

In total, 2.2 million jets of each jet type are produced. Their transverse momentum, p_T , and direction is determined by summing the four-vectors of all jet constituents that have their origin in the primary vertex. To remove small kinematic differences between s - and d -jets, the p_T and pseudorapidity (η) distributions of the d -jets are reweighted to match the distributions of the s -jets.

All jet constituents are ordered by energy unless mentioned otherwise. The number of constituent particles per jet is shown in Figure 1. The distribution is similar for s - and d -jets with an average of 13.4 particles and a standard deviation of 4.9 particles. Because only a very small fraction of jets has more than 50 constituent particles, any additional particles are not considered in the following.

Figure 2 shows the mass and the type of the leading constituent particle in the jets. For s -jets, the leading particle tends to be a strange-hadron (mostly kaons), while for d -jets, the leading particle is more likely to be a light hadron — in particular a pion. While, on average, the type of the leading particle differs between s - and d -jets, its kinematic properties are similar. As an example, the transverse momentum of the leading particle is shown in Figure 3. The leading particles of s -jets tend to carry only slightly more momentum than those of d -jets. This is in line with the fact that kaons produced in pp collisions tend to have larger transverse momentum as known from fragmentation functions determined at the same center-of-mass energy [61].

Some differences between s - and d -jets are, for example, observed in the width of the jets, which is defined as

$$\text{jet width} = \frac{\sum_i p_T^i \Delta R(i, \text{jet})}{\sum_i p_T^i}, \quad (2.1)$$

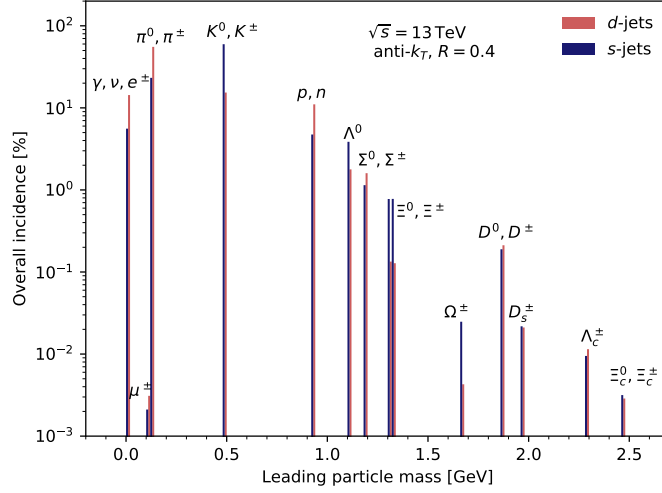


Figure 2. Mass spectrum of the jets' constituent particle leading in energy for s - and d -jets.

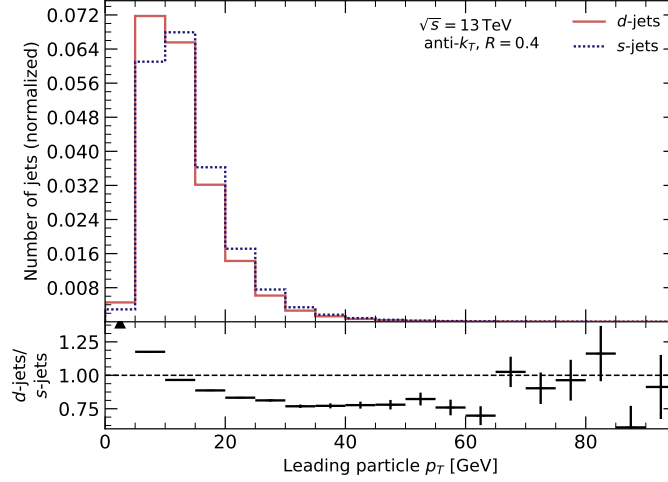


Figure 3. Distribution of the energy of the jets' constituent particle leading in energy for s - and d -jets.

where i runs over all particles in the jet and

$$\Delta R(i, \text{jet}) = \sqrt{(\phi_{\text{jet}} - \phi_i)^2 + (\eta_{\text{jet}} - \eta_i)^2} \quad (2.2)$$

is based on the differences in azimuthal angle (ϕ) — in the transverse plane perpendicular to the beam axis — and in pseudorapidity of the particle and the jet. The jet width, as shown in Figure 4, tends to be on average slightly more narrow for s -jet than for d -jets. However, the comparison of the two distributions also demonstrates that even complex and engineered features, like the jet width, have little discrimination power, which makes s -tagging a challenging task.

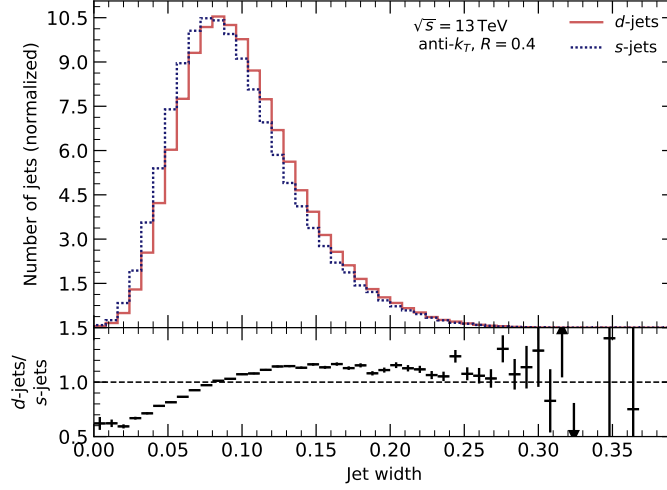


Figure 4. Distribution of the jet width of s - and d -jets.

3 Detector scenarios

A total of ten scenarios with different combinations of ideal detector components are studied. Each scenario is characterized by a different selection of the input features for the neural network which correspond to those properties of the jets that the detector components are designed to measure. For example, in a scenario with a tracking detector, the momentum, trajectory, and charge of charged particles are used as input features. However, detector effects, like alignment, hit inefficiencies, track reconstruction, momentum resolution, charge misidentification, and hadron-collision-related effects such as pile-up or beam remnant are not taken into account. All of them are expected to reduce the performance of an s -tagger. In the following, all ten scenarios are briefly described and motivated. An overview of all scenarios as well as a summary of the input features is given in Table 1. All scenarios have in common, that the jet p_T , η , and ϕ are always used as input to the neural network.

3.1 Ideal detectors

3.1.1 Universal collider detector

This scenario corresponds to an ideal detector, that would be able to identify and measure the properties of all jet constituents with infinite precision. While this is of course unrealistic, this scenario helps to determine an upper bound on the performance that an s -tagger can possibly achieve.

All constituent particles of the jets are used as input to the recurrent neural network. Only particles with zero lifetime are rejected because they do not enter the jet reconstruction algorithm. The neural network is provided with a set of nine input variables which fully describe the particles' properties: The particles' four-momenta are described by their energy E , pseudorapidity η , azimuthal angle ϕ , and mass m . In addition, the linear trajectory of the particles is fully determined by their point of creation (either the primary vertex or secondary decay vertices defined by the radial distance from the primary vertex r_0 and the angles η_0 and ϕ_0), as well as the direction of the

Name	Selection criteria	Input variables
Universal detector	$\tau > 0$	E, η, ϕ, m (4-momentum) r_0, η_0, ϕ_0 (origin) τ (lifetime in lab system) q (charge)
Universal detector excluding beampipe	$\tau > 0$ $r_f > 10 \text{ mm}$	E, η, ϕ, m (4-momentum), r_i, η_i, ϕ_i (initial measurement), τ (lifetime in lab system), q (charge)
Infinite tracker	$\tau > 0$ $r_f > 10 \text{ mm}$ $q \neq 0$	p, η, ϕ (4-momentum minus mass) r_i, η_i, ϕ_i (initial measurement) τ (lifetime in lab system) q (charge)
Finite tracker	$\tau > 0$ $r_f > 10 \text{ mm}$ $q \neq 0$ $r_0 < 1 \text{ m}$	p, η, ϕ (4-momentum minus mass) r_i, η_i, ϕ_i (initial measurement) τ (lifetime in lab system) q (charge)
Cherenkov tracker	$\tau > 0$ $r_f > 10 \text{ mm}$ $q \neq 0$ $r_0 < 1 \text{ m}$	p, η, ϕ, m (4-momentum) r_i, η_i, ϕ_i (initial measurement) τ (lifetime in lab system) q (charge)
Calorimeter without ECAL/HCAL separation	$\tau > 0$ $r_0 < 1 \text{ m}$ $r_f > 1 \text{ m}$ no ν	E, η, ϕ (3-momentum)
Calorimeter with ECAL/HCAL separation	$\tau > 0$ $r_0 < 1 \text{ m}$ $r_f > 1 \text{ m}$ no ν	E, η, ϕ (3-momentum), particle category ($\gamma/e, \mu$, other)
Finite tracker, no $0 \rightarrow + -$ decays	$\tau > 0$ $r_f > 10 \text{ mm}$ $r_0 < 1 \text{ m}$ $q \neq 0$ no charged particles from neutral decays	p, η, ϕ, m (4-momentum) r_i, η_i, ϕ_i (initial measurement) τ (lifetime in lab system) q (charge)
Finite tracker, only $0 \rightarrow + -$ decays	$\tau > 0$ $r_f > 10 \text{ mm}$ $r_0 < 1 \text{ m}$ $q \neq 0$ only charged particles from neutral decays	p, η, ϕ, m (4-momentum) r_i, η_i, ϕ_i (initial measurement) τ (lifetime in lab system) q (charge)

Table 1. List of all considered detector scenarios as a combination of ideal detector components. The second column shows the selection requirements imposed on the particles used as input to the neural networks, where τ means the lifetime of the particles, r_0 is the radial distance between the primary vertex and the point where the particle is created, and r_f is the radial distance between the primary vertex and the decay vertex. The third column describes the variables that are used as inputs to the neural network. If the variable carries a subscript 0, it refers to the spacepoint of creation, and if it carries a subscript i , it refers to the spacepoint of initial measurement.

four-momentum vector and the lifetime τ . Finally, for an unambiguous identification of the particle type, the charge q of the particles is used as input variable.

3.1.2 Universal collider detector excluding the beampipe

A detector is usually not able to measure particles arbitrarily close to the primary vertex because it is at least limited by the radius of the beampipe. In order to take this aspect into account, the input to the neural network is modified by removing all truth particle that decay within a radius of $r = 10$ mm. The value of the radius is inspired by the size of the beampipe at the Large Hadron Collider experiments. In addition, if particles are created within the beampipe, the values of their point of creation (r_0, η_0, ϕ_0) are altered to represent the point of initial detection. Furthermore, if the particle has a finite lifetime, the time it takes for the particle to travel from the point of creation to the point of initial detection is subtracted from the lifetime measured in the laboratory frame.

3.1.3 Infinite and finite tracking detectors

In most collider detectors, the tracking detector is the detector with the best spacial resolution. It measures so-called hits when charged particles pass through its active material, which is often structured in layers. The hits are then connected using track reconstruction algorithms to reconstruct the charged particles' trajectories. The momentum of the particle and sign of its electric charge are determined from the curvature of the track in a magnetic field.

Since tracking detectors measure only charged particles, in the following scenarios, these are the only particles which are passed to the neural network as input. Since tracking detectors measure the particles' three-momentum and electric charge², the mass m is not included as an input feature, and the particle momentum p is used instead of the energy. Since this is an ideal tracking detector, no track reconstruction inefficiencies or resolutions for the momenta and angles are considered.

To investigate whether the radial size of the tracking detector is important, a scenario with an infinite detector (starting at $r = 10$ mm and extending out indefinitely) and a scenario with a detector with $10 \text{ mm} < r < 1 \text{ m}$ are compared. In both cases, the point of initial detection (r_0, η_0, ϕ_0) as well as the measured lifetime (τ) are modified as described previously for the universal collider detector excluding the beampipe. If any particle decays within the radius of $r = 10$ mm or — in case of the finite detector — has its origin beyond a radius of $r = 1$ m, it is removed from the list of input particles. It has to be mentioned that this scenario is not able to cover the impact of K_L decays since Pythia considers them as stable. Therefore, a large difference between the finite and the infinite tracker scenario is not expected.

3.1.4 Cherenkov tracking detector

In the past, Cherenkov detectors were used to identify charged kaons in order to discriminate s -jets from other jets [40, 41]. Using the emission of Cherenkov light and the momentum measurement from the tracking detectors, Cherenkov detectors distinguish between charged particles with different masses. Similarly, the energy loss in a tracking detector (dE/dx) in combination with the measurement of the momentum can be used to determine the mass of a charged particle. Both of

²It is assumed that all particles carry either unit electric charge or are electrically neutral, which is true for all relevant leptons and hadrons. Hence, the charge is inferred from the measurement of the sign of the charge.

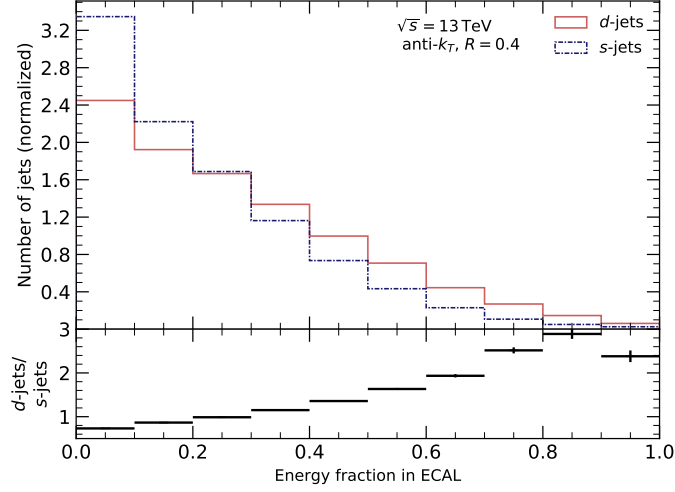


Figure 5. Distribution of the fraction of jet energy that is deposited in the ECAL, i.e. the fraction of energy carried by electrons and photons, for s -jets and d -jets.

these methods typically have limitations for large momenta. However, in this idealized detector scenario, a detector that is able to perfectly measure the mass and three-momentum of charged particles is assumed. Similar to the finite tracking detector, the detector covers the space within a radius of $10 \text{ mm} < r < 1 \text{ m}$. The only difference is that the particles' masses are used as an additional input feature.

3.1.5 Calorimeters with and without separation into electromagnetic and hadronic components

Calorimeters measure the energy of electrons and photons via electromagnetic showers and the energy of both charged and neutral hadrons via hadronic showers. Typically, two separate types of calorimeters are used, one that is optimized for electromagnetic showers (ECAL) and one that is optimized for hadronic showers (HCAL).

One feature that can be used to discriminate s - and d -jets is the fraction of energy that is deposited in the ECAL. Jets from down quarks tend to contain more photons from $\pi^0 \rightarrow \gamma\gamma$ decays, while s -jets tend to contain more K_L mesons, which typically do not decay before they reach the calorimeters. Figure 5 illustrates the fraction of energy of a jet carried by photons and electrons — as would be measured by a perfect ECAL — for both s -jets and d -jets at a radius of $r = 1 \text{ m}$, where the distance of 1 m from the primary vertex is inspired by calorimeters at the Large Hadron Collider.

Moreover, the geometrical distribution of energy within the jets (substructure) could contain additional information for the discrimination of s -jets and d -jets. To evaluate the discrimination power of both, substructure and energy fraction carried by electrons and photons, two calorimeter scenarios are considered.

The first scenario is a calorimeter without separation into ECAL and HCAL, which can perfectly determine the energy and angles in the η - ϕ plane of a particle. The input to the neural network is the energy E , pseudorapidity η , and azimuthal angle ϕ at the radius $r = 1 \text{ m}$ for all particles that

pass through this radius, except for neutrinos ν . This scenario is sensitive to the discrimination power of the jet substructure.

A second calorimeter scenario passes an additional variable to the neural network which discriminates between three different particle categories: (1) electrons and photons, (2) muons, which are minimum ionizing particles that typically pass through the calorimeters and are then identified with muon detectors that are situated behind the calorimeters, and (3) all other particles, including foremost hadrons but also tau leptons. This emulates the classification of particles with a combination of ECAL and HCAL. Any increase in separation power with respect to the first calorimeter scenario can therefore be attributed to the separation of electromagnetic and hadronic energy deposits and — to a lesser extent — the presence of muons.

3.2 Strange-hadron decays to two charged particles

It is possible to reconstruct decays of neutral strange-hadrons to two charged particles, such as $K_S \rightarrow \pi^+\pi^-$ or $\Lambda^0 \rightarrow p\pi^-$, using a tracking detector. As such strange-hadrons are more prevalent in s -jets than in d -jets, it is worth asking how much discrimination power is contained in these $0 \rightarrow ++$ decays.

To estimate the separation power from $0 \rightarrow ++$ decays, the input to the finite tracker scenario is modified to exclusively contain pairs of oppositely charged particles that come from the decay of a neutral particle. In a complementary approach, a selection is applied that removes these opposite-sign pairs from the finite-tracker input.

This study is additionally used to cross check the ordering of the particle input by their energy. For the LSTM networks, the reconstruction of $0 \rightarrow ++$ decays may be easier if the input particles are ordered by their radius of the first measurement (r_0) instead of their energy [42], since the two charged particles would be close to each other in the input. If only little performance is gained by changing from the energy ordering to an ordering in r_0 for the training, this would suggest that secondary vertices can be reconstructed independently of whether the constituents are ordered by r_0 or E .

4 Neural-network architecture

For each scenario, the input features as discussed in the previous section are used. All input features are preprocessed ensuring that they lie in a comparable range using scikit-learn’s [62] RobustScaler, which centers the distributions around zero and divides them by the range between their first and third quartiles. The full data set of jets is split into a training sample (3/5), a validation sample (1/5) to monitor the neural network performance during the training and hyperparameter optimization, and an independent test sample (1/5) to evaluate the performance after the training.

The neural networks are implemented with Keras [63] using TensorFlow [64] as backend. Figure 6 illustrates the neural networks’ architecture. Their input layers contain as many nodes as there are constituent-level input features used in the respective scenario, that means for example nine input nodes for the universal-collider-detector scenario and three input nodes for the calorimeter scenario without separation into electromagnetic and hadronic components. These input nodes are connected to the first LSTM layer. The remaining part of all neural networks are structured in the same way for all scenarios and consist of two LSTM layers with 64 and 32 units followed by two

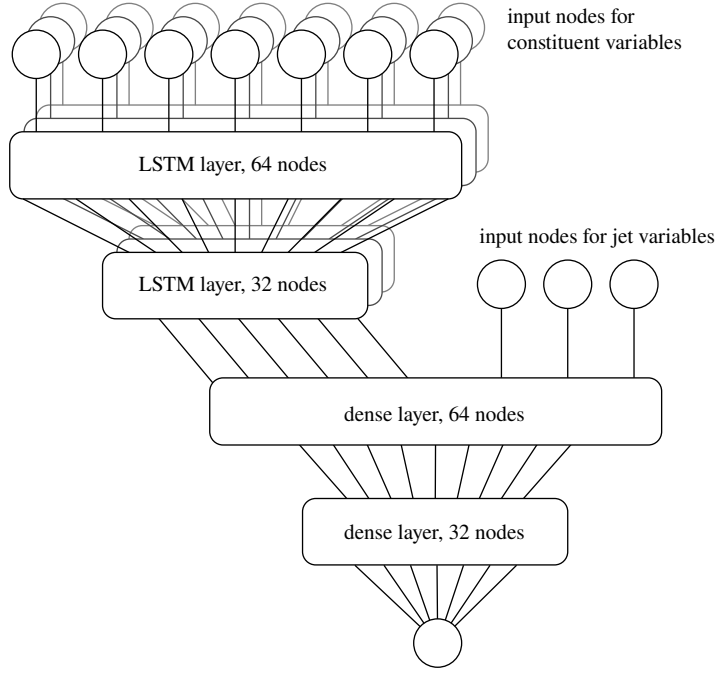


Figure 6. Visualisation of the neural network architecture used. Circles visualise input and output nodes, while boxes illustrate both LSTM and dense layers. The number of connections between layers illustrated as lines does not represent the number of connections.

fully-connected feed-forward (dense) layers with 64 and 32 nodes and a single output node. In addition to the 32 output nodes from the second LSTM layer, the p_T , η , and ϕ of the jet are fed to the first dense layer. This configuration ensures that the capacity of the neural network is large enough in all scenarios. For example, removing one LSTM layer decreases the overall performance of the neural networks significantly, while adding another LSTM layer only results in stronger overtraining, but not in an increased performance, when the network is regularized sufficiently. An L_2 -norm penalty term is applied to weights of recurrent connections and to weights connecting each hidden layer in order to regularize the network. The same regularization strength is applied to each layer, but the value is optimized for each of the detector scenarios in order to find the optimal effective capacity by minimizing overtraining and maximizing the performance.

In both LSTM layers, the hyperbolic tangent function is used as activation for all gates, except for the recurrent connections, for which the sigmoid function is used. All nodes of the dense hidden layers are activated using the rectified linear unit, while the output node is activated using the sigmoid function.

During the training process, the binary cross entropy is optimized by the Adam algorithm [65] with an initial learning rate of 0.001 and a batch size of 1024 jets.

To evaluate the performance of the neural networks, modified receiver operating characteristic (ROC) curves are used, which show the relation between signal efficiency ($\varepsilon_{s\text{-jets}}$) and background rejection ($1/\varepsilon_{d\text{-jets}}$) for any cut on the output distribution of the neural network. As performance metric, the area under the curve (AUC) of the ROC curve is used, which can take on any value

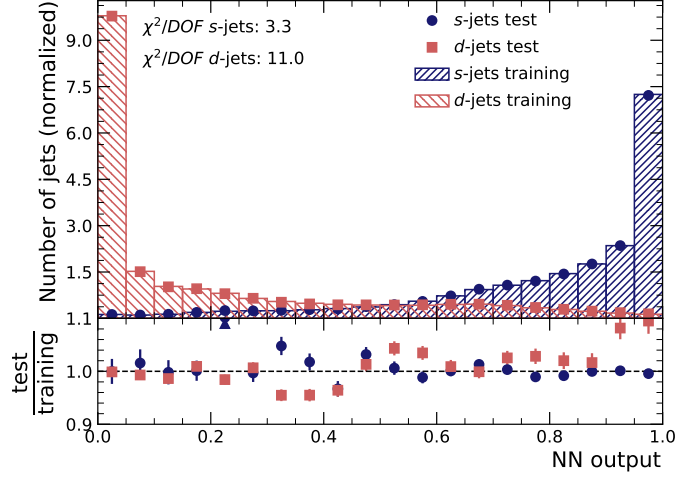


Figure 7. Output distribution of the neural network in the universal detector scenario. The output for the training sample as well as for the independent test sample is compared for s -jets and d -jets.

between 0.5 (no separation) and 1.0 (perfect separation) and is calculated with scikit-learn’s [62] AUC score. As an additional regularization measure, early stopping is used, which is triggered if the AUC value of the validation set has not improved by more than 0.0001 over the course of 20 epochs. The neural network model of the epoch with the largest AUC value on the validation set is used to evaluate the final performance of the neural network.

5 Results

In the following, the classification performances of all ideal detector scenarios are discussed and compared. The comparison is divided into four different subsections: A comparison of (1) perfect detectors that can reconstruct all particles, (2) ideal tracking and Cherenkov detectors, (3) ideal calorimeter detectors, and (4) a comparison of different scenarios with neutral-to-charged-particles decays.

5.1 Universal collider detectors

Figure 7 shows the output distributions of the neural network trained in the scenario of the universal detector. s -jets and d -jets are separated well, forming two distinct peaks around values of 0 for d -jets and 1 for s -jets, which means many jets can be clearly identified correctly as d -jets and s -jets. The comparison between the output of the training sample and the independent test sample shows that there is no indication of strong overtraining, i.e. there is no clear bias visible in the ratio between the test and training data set.

Figure 8 compares the ROC curves of the universal detector with the universal detector that excludes the beampipe. For the full range of signal efficiencies, the classification power of both scenarios is very similar. The statistical uncertainty is evaluated by bootstrapping the test sample, i.e. generating a sample of the same size by drawing with replacement. The AUCs of 0.938 ± 0.001 for the universal detector and 0.938 ± 0.001 for the universal detector that excludes the beampipe

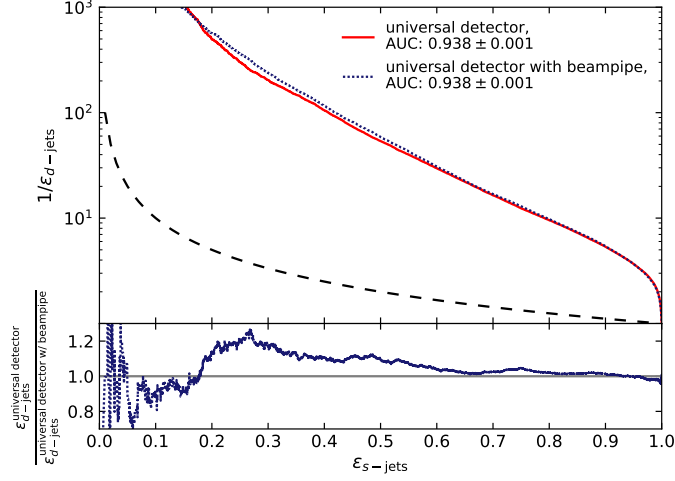


Figure 8. ROC curves illustrating the classification power of neural networks of the universal detector scenario and the universal detector scenario that excludes the beampipe. The signal is composed of s -jets, and the background is composed of d -jets. The dashed line illustrates a ROC curve for the case of no separation. The ratio beneath the ROC curves shows the efficiency of d -jets in the universal detector scenario excluding the beampipe divided by the efficiency of d -jets in the universal detector scenario. The efficiencies are evaluated on the test sample and the uncertainty in the area under the curve is the statistical uncertainty associated with that sample.

agree within the uncertainties. This indicates that only little information is lost by not covering the innermost volume around the primary vertex, which is consistent with the fact that the average number of particles per s -jet (d -jet) drops only slightly from 13.4 (13.4) to 12.5 (12.6).

The classification power achieved in these scenarios is significantly larger than those achieved in Refs. [42] and [43], which included a detector simulation. This means that, while the hadronisation patterns of s - and d -jets differ, the differences are significantly reduced by detector effects, such as resolutions and inefficiencies. The goal of the following studies with the other ideal detector scenarios is to evaluate which type of detector may provide the largest potential for exploiting the differences between s - and d -jets.

5.2 Tracking and Cherenkov detectors

The output distributions of the neural network in the infinite-tracker scenario is shown in Figure 9. There is no indication of strong overtraining by comparing the output of the test and training set. The separation between s -jets and d -jets is not as strong as in the universal-detector scenario. While there is still a strong but less pronounced peak around 0 for d -jets, there is no such peak around 1 for s -jets, meaning their defining characteristics are much less unambiguous with a tracking detector. Moreover, a peak around 0.5 in the center of the output distribution is observable for both jet flavours, indicating that with only the information of charged particles available, some s - and d -jets are not well separable.

As shown in the ROC curves of Figure 10, all three tracking scenarios perform quite similarly. With an AUC of 0.795 ± 0.001 , the finite and the infinite tracking scenarios have the same separation power. Given that in Pythia, hadrons that very rarely decay before entering the calorimeters, such

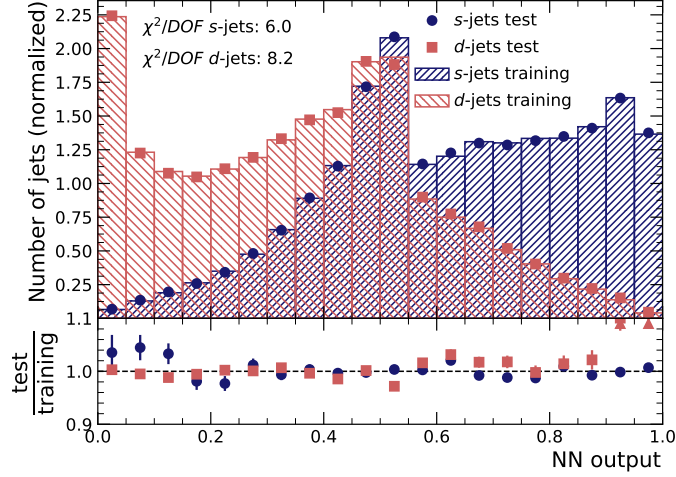


Figure 9. Output distribution of the neural network in the infinite-tracker scenario. The output for the training sample as well as for the independent test sample is compared for s -jets and d -jets.

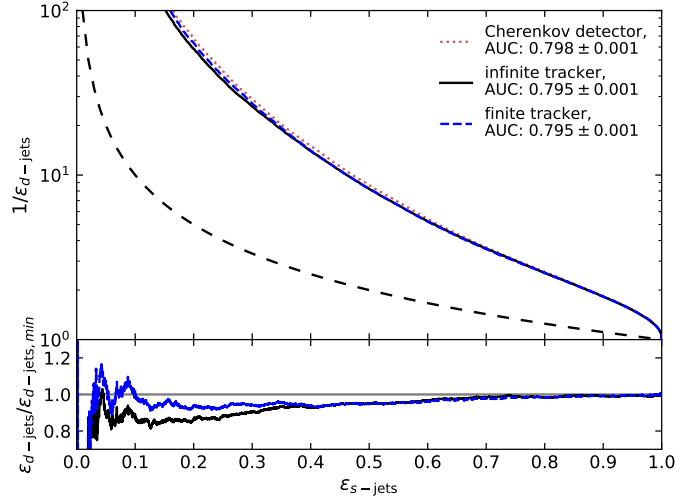


Figure 10. ROC curves illustrating the classification power of neural networks of the infinite tracker, the finite tracker, and the Cherenkov tracking detector. The signal is composed of s -jets, and the background is composed of d -jets. The dashed line illustrates a ROC curve for the case of no separation. The ratio beneath the ROC curves shows the efficiency for d -jets in one scenario ($\epsilon_{d\text{-jets}}$) divided by the efficiency for d -jets in the scenario with the best separation power shown in the ROC curve ($\epsilon_{d\text{-jets,min}}$). The efficiencies are evaluated on the test sample and the uncertainty in the area under the curve is the statistical uncertainty associated with that sample.

as the K_L meson, are treated as stable particles, this result is expected. Adding the ideal Cherenkov detector and thus the capability of identifying constituent particles by their mass improves the AUC only slightly to 0.798 ± 0.001 , but it does help to increase the background rejection rate over the full signal efficiency range.

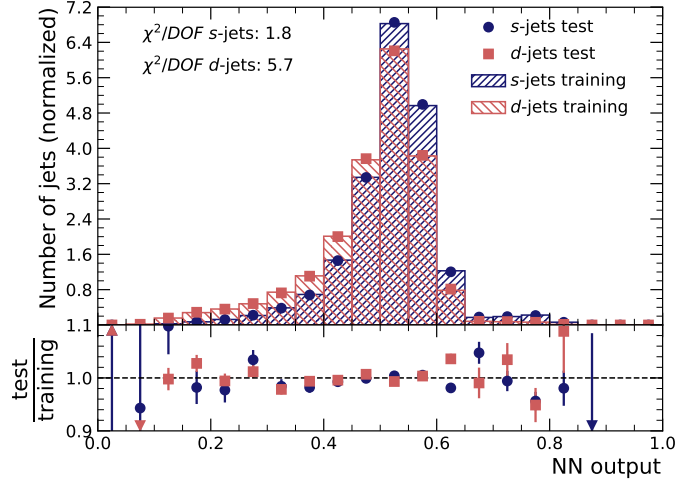


Figure 11. Output distribution of the neural network in the calorimeter scenario with separate ECAL and HCAL components. The output for the training sample as well as for the independent test sample is compared for s -jets and d -jets.

Ref. [42] also used tracks, but considered a simplified detector simulation with Delphes [66], which resulted in roughly seven times more d -jets for an s -tagging efficiency of 30% compared to Figure 10 and two times more d -jets for an s -tagging efficiency of 70%, i.e. background efficiencies that are seven and two times larger respectively than in the finite tracker scenario. The largest effect probably originates from the finite tracking efficiencies in Ref. [42] — which vary between 60% and 95% depending on the track’s p_T and η — as well as resolution effects.

5.3 Calorimeters

Figure 11 shows the output distribution of the neural network in the calorimeter scenarios with separation into ECAL and HCAL components. There is no indication of strong overtraining by comparing the response of the test and training set. The separation between s -jets and d -jets is strongly degraded compared to the previously discussed scenarios, and both jet types respond mostly with an output value around 0.5, which indicates that it is very difficult for the neural network to distinguish the two classes.

Figure 12 compares the ROC curves of both calorimeter scenarios with a ROC curve obtained only from the distribution of the fraction of energy deposited by electrons and photons, as shown in Figure 5. The classification power of the network trained with the scenario without a calorimeter separation is significantly smaller with an AUC value of 0.544 ± 0.001 than the one trained with ECAL and HCAL components, which results in an AUC value of 0.600 ± 0.001 . This indicates that the separation power is mostly driven by the share of energies between the ECAL and HCAL components instead of the spatial pattern of the energy depositions. This hypothesis is supported by the ROC curve that is constructed only from the energy fraction of electrons and photons, which results in an AUC value of 0.584 ± 0.001 , which is almost as good as the one of the ideal calorimeter scenario with a separation into ECAL and HCAL.

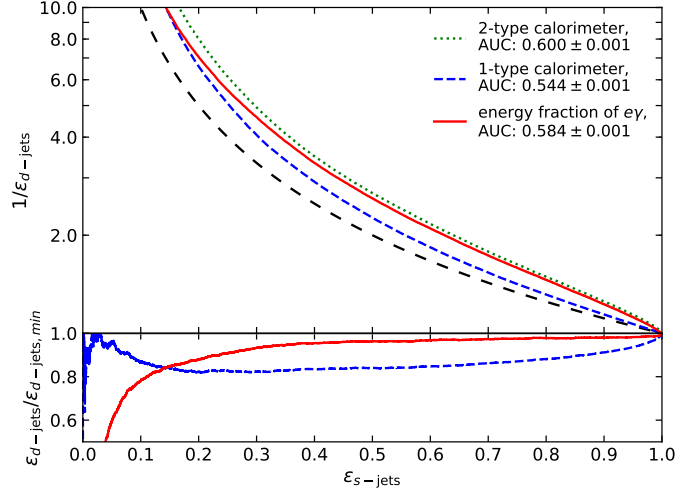


Figure 12. ROC curves illustrating the classification power of neural networks in the calorimeter scenarios with (“2-type”) and without (“1-type”) separation into ECAL and HCAL components, as well as the ROC curve of the fraction of energy deposited by electrons and photons. The signal is composed of s -jets, and the background is composed of d -jets. The dashed line illustrates a ROC curve for the case of no separation. The ratio beneath the ROC curves shows the efficiency for d -jets in one scenario ($\epsilon_{d\text{-jets}}$) divided by the efficiency for d -jets in the scenario with the best separation power shown in the ROC curve ($\epsilon_{d\text{-jets,min}}$). The efficiencies are evaluated on the test sample and the uncertainty in the area under the curve is the statistical uncertainty associated with that sample.

5.4 Strange-hadron decays to two charged particles

Figure 13 compares ROC curves illustrating the classification performances of the neural network trained with the input of the finite tracker scenario with networks trained on subsets of the scenario’s inputs. As discussed in Section 3.2, the aim of this comparison is to determine the separation power in strange-hadron decays to two charged particles, in particular $K_S \rightarrow \pi^+ \pi^-$. If the neural network is only trained with charged particles from these decays as input, the AUC value drops to 0.653 ± 0.001 in comparison to 0.795 ± 0.001 for the finite tracker scenario. This is mainly due to the facts that only about one quarter of all kaons are K_S mesons and that K_S mesons decay in only roughly 70% of the cases into $\pi^+ \pi^-$.

However, if the neural network is trained with the orthogonal subset of particles as input (i.e. including all charged particles except for those that come from the decay of a neutral particle), the AUC is 0.728 ± 0.001 . This shows that the larger part of the differences between s - and d -jets in their track properties is not based on the decays of neutral strange-hadrons.

As there are no constituent particles with a charge other than 0 or ± 1 , when looking at tracks produced by charged particles, there are only three different types of particle signatures: (1) neutral particle decays to two particles of opposite-sign electric charge (and possibly other neutral particles), (2) charged particle decays into one or more neutral particles and one charged particle (or another odd number of charged particles), and (3) stable charged particles. When the neutral particle decays are excluded from the training sample, the separation power therefore has to be driven by either a charged particle decaying into one charged and one or more neutral particles or stable charged

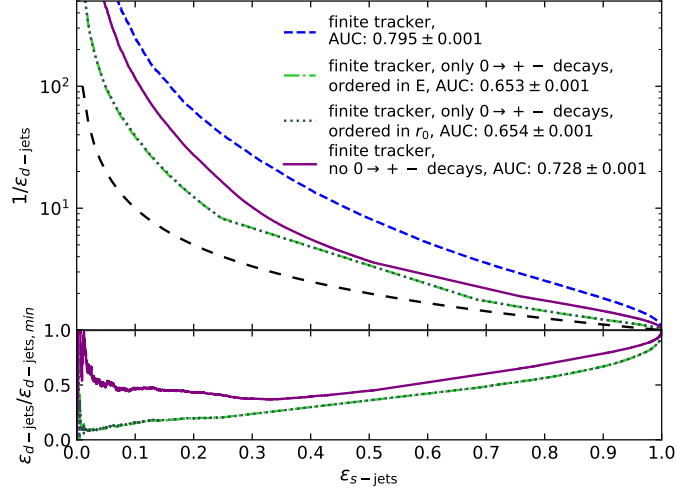


Figure 13. ROC curves illustrating the classification power of the finite-tracker scenario in comparison to scenarios where the input excludes particles from $0 \rightarrow + -$ decays or only includes particles from these decays. For the latter case, also an additional ordering in r_0 instead of energy is shown. The signal is composed of s -jets, and the background is composed of d -jets. The dashed line illustrates a ROC curve for the case of no separation. The ratio beneath the ROC curves shows the efficiency for d -jets in one scenario ($\varepsilon_{d\text{-jets}}$) divided by the efficiency for d -jets in the scenario with the best separation power shown in the ROC curve ($\varepsilon_{d\text{-jets,min}}$). The efficiencies are evaluated on the validation test sample and the uncertainty in the area under the curve is the statistical uncertainty associated with that sample.

particles. The former signature would be visible as a number of particles with an initial radius $r > 10$ mm. However, the number of these particles is very low and cannot explain the separation power observed without the $0 \rightarrow + -$ decays. Therefore, this separation power must be driven by the substructure of stable charged particles.

Figure 13 also shows the comparison of the neural network trained with the $0 \rightarrow + -$ input particles sorted by the radius of their initial measurement, r_0 , in addition to the default ordering, i.e. by the particle energy. Both networks have a comparable discrimination power, suggesting that the LSTM is stable under this change in particle ordering.

6 Conclusions

Achieving good performance for s -tagging, i.e. the separation of s -jets from other light jets, is challenging. This is in part due to similarities in the fragmentation of s - and d - or u -jets and in part due to experimental challenges. In order to separate these two effects, the performance of s -tagging based on idealised detector scenarios was studied. Long short-term memory recurrent neural networks were used as a complex model designed to capture the differences in the jet constituents in the different scenarios.

An overview of the performance of the three main scenarios is shown in Figure 14. Assuming an ideal detector that can perfectly measure all jet constituents (“universal collider detector”), s - and d -jets can be separated well. This means that the fragmentation of s - and d -jets shows promising differences that may be explored in an s -tagging algorithm, but that the maximum

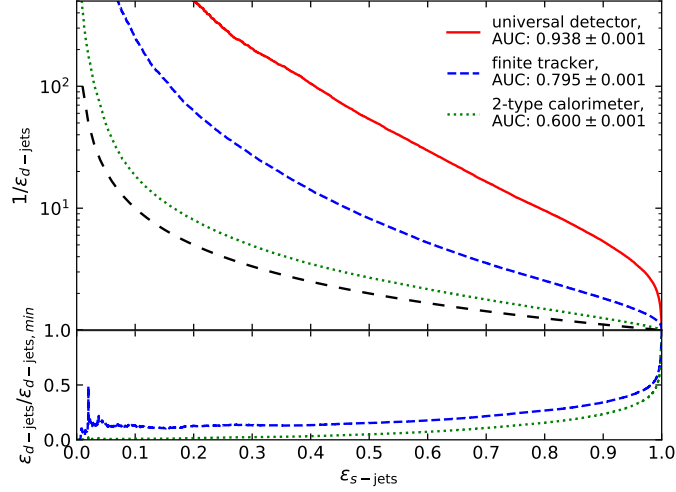


Figure 14. ROC curves illustrating the classification power of the neural networks in the universal-detector, finite-tracker, and ECAL/HCAL-separated calorimeter (“2-type calorimeter”) scenarios. The signal is composed of s -jets, and the background is composed of d -jets. The dashed line illustrates a ROC curve for the case of no separation. The ratio beneath the ROC curves shows the efficiency for d -jets in one scenario ($\epsilon_{d\text{-jets}}$) divided by the efficiency for d -jets in the scenario with the best separation power shown in the ROC curve ($\epsilon_{d\text{-jets,min}}$). The efficiencies are evaluated on the test sample and the uncertainty in the area under the curve is the statistical uncertainty associated with that sample.

achievable performance of an s -tagger is by far not as good as for example achieved for b -tagging algorithms [2, 3]. The comparison also shows that the information measured in a perfect tracker may be much more valuable for s -tagging than the energy deposits measured in electromagnetic and hadronic calorimeters.

However, realistic detectors are subject to a reduced fiducial acceptance, reconstruction inefficiencies, and resolutions for the different input features that are used for the training of the s -tagger. While our studies show a larger potential for s -tagging based on tracking information than based on calorimeter information, it was shown that the main discriminatory power does not stem from the reconstruction of the decays of neutral strange-hadrons, as they represent only a limited fraction of the leading jet constituents in s -jets. In addition, track reconstruction is subject to important inefficiencies — in particular at low track p_T — which further reduce the efficacy of a separation based on tracks. Interestingly, the addition of an ideal Cherenkov detector to the tracking scenario does not yield a large improvement. Calorimeter measurements are subject to a limited granularity and to significant resolution effects in the energy measurement. The main discriminatory power, however, was found not to be in the geometric structure of the energy deposits but in the fraction that is carried by electrons and photons. While this fraction is subject to significant fluctuations in the development of hadronic showers (in particular the fraction of high-energy π^0 mesons, which result in electromagnetic subshowers) and thus has limited resolution, it is a much simpler variable than the complex combination of particle momenta in the LSTM neural network.

While the maximum performance of an s -tagging algorithm is limited, its development allows for new opportunities in data analysis at colliders. The results of the ideal-detector scenarios

underline the importance of following a two-fold approach to s -tagging, based on tracking [42] and calorimeter information [43]. In order to gauge the performance of s -taggers in realistic scenarios, the performance achieved in the scenario with the universal collider detector is proposed as a benchmark, which is solely based on the difference in s - and d -quark fragmentation.

Acknowledgments

These studies have been financially supported by the Studienstiftung des deutschen Volkes. Special thanks to Nils Julius Abicht for generating the simulated samples used in this study and to Tomas Dado for his comments on the manuscript.

References

- [1] DELPHI collaboration, *Measurement of the rate of $b\bar{b}b\bar{b}$ events in hadronic Z decays and the extraction of the gluon splitting into $b\bar{b}$* , *Phys. Lett. B* **462** (1999) 425.
- [2] ATLAS collaboration, *ATLAS b -jet identification performance and efficiency measurement with $t\bar{t}$ events in pp collisions at $\sqrt{s} = 13$ TeV*, *Eur. Phys. J. C* **79** (2019) 970, [[1907.05120](#)].
- [3] CMS collaboration, *Identification of heavy-flavour jets with the CMS detector in pp collisions at 13 TeV*, *JINST* **13** (2018) P05011, [[1712.07158](#)].
- [4] ATLAS collaboration, *Search for the Decay of the Higgs Boson to Charm Quarks with the ATLAS Experiment*, *Phys. Rev. Lett.* **120** (2018) 211802, [[1802.04329](#)].
- [5] J. Pumplin, *How to tell quark jets from gluon jets*, *Phys. Rev. D* **44** (1991) 2025–2032.
- [6] CMS collaboration, “Performance of quark/gluon discrimination in 8 TeV pp data.” CMS-PAS-JME-13-002, <https://cds.cern.ch/record/1599732>, 2013.
- [7] ATLAS collaboration, G. Aad et al., *Light-quark and gluon jet discrimination in pp collisions at $\sqrt{s} = 7$ TeV with the ATLAS detector*, *Eur. Phys. J. C* **74** (2014) 3023, [[1405.6583](#)].
- [8] P. T. Komiske, E. M. Metodiev and M. D. Schwartz, *Deep learning in color: towards automated quark/gluon jet discrimination*, *JHEP* **01** (2017) 110, [[1612.01551](#)].
- [9] T. Cheng, *Recursive Neural Networks in Quark/Gluon Tagging*, *Comput. Softw. Big Sci.* **2** (2018) 3, [[1711.02633](#)].
- [10] E. M. Metodiev, B. Nachman and J. Thaler, *Classification without labels: Learning from mixed samples in high energy physics*, *JHEP* **10** (2017) 174, [[1708.02949](#)].
- [11] L. M. Dery, B. Nachman, F. Rubbo and A. Schwartzman, *Weakly Supervised Classification in High Energy Physics*, *JHEP* **05** (2017) 145, [[1702.00414](#)].
- [12] E. M. Metodiev and J. Thaler, *Jet Topics: Disentangling Quarks and Gluons at Colliders*, *Phys. Rev. Lett.* **120** (2018) 241602, [[1802.00008](#)].
- [13] P. T. Komiske, E. M. Metodiev and J. Thaler, *An operational definition of quark and gluon jets*, *JHEP* **11** (2018) 059, [[1809.01140](#)].
- [14] P. T. Komiske, E. M. Metodiev and J. Thaler, *Energy Flow Networks: Deep Sets for Particle Jets*, *JHEP* **01** (2019) 121, [[1810.05165](#)].
- [15] G. Kasieczka, N. Kiefer, T. Plehn and J. M. Thompson, *Quark-Gluon Tagging: Machine Learning vs Detector*, *SciPost Phys.* **6** (2019) 069, [[1812.09223](#)].

- [16] V. Mikuni and F. Canelli, *ABCNet: An attention-based method for particle tagging*, *Eur. Phys. J. Plus* **135** (2020) 463, [[2001.05311](#)].
- [17] G. Kasieczka, S. Marzani, G. Soyez and G. Stagnitto, *Towards Machine Learning Analytics for Jet Substructure*, *JHEP* **09** (2020) 195, [[2007.04319](#)].
- [18] ATLAS collaboration, *Identification of high transverse momentum top quarks in pp collisions at $\sqrt{s} = 8$ TeV with the ATLAS detector*, *JHEP* **06** (2016) 093, [[1603.03127](#)].
- [19] G. Kasieczka, T. Plehn, M. Russell and T. Schell, *Deep-learning Top Taggers or The End of QCD?*, *JHEP* **05** (2017) 006, [[1701.08784](#)].
- [20] A. Butter, G. Kasieczka, T. Plehn and M. Russell, *Deep-learned Top Tagging with a Lorentz Layer*, *SciPost Phys.* **5** (2018) 028, [[1707.08966](#)].
- [21] ATLAS collaboration, *Performance of top-quark and W-boson tagging with ATLAS in Run 2 of the LHC*, *Eur. Phys. J. C* **79** (2019) 375, [[1808.07858](#)].
- [22] S. Macaluso and D. Shih, *Pulling Out All the Tops with Computer Vision and Deep Learning*, *JHEP* **10** (2018) 121, [[1803.00107](#)].
- [23] B. M. Dillon, D. A. Faroughy and J. F. Kamenik, *Uncovering latent jet substructure*, *Phys. Rev. D* **100** (2019) 056002, [[1904.04200](#)].
- [24] S. Diefenbacher, H. Frost, G. Kasieczka, T. Plehn and J. M. Thompson, *CapsNets Continuing the Convolutional Quest*, *SciPost Phys.* **8** (2020) 023, [[1906.11265](#)].
- [25] CMS collaboration, *Identification of heavy, energetic, hadronically decaying particles using machine-learning techniques*, *JINST* **15** (2020) P06005, [[2004.08262](#)].
- [26] A. Chakraborty, S. H. Lim, M. M. Nojiri and M. Takeuchi, *Neural Network-based Top Tagger with Two-Point Energy Correlations and Geometry of Soft Emissions*, *JHEP* **20** (2020) 111, [[2003.11787](#)].
- [27] CMS collaboration, *Identification techniques for highly boosted W bosons that decay into hadrons*, *JHEP* **12** (2014) 017, [[1410.4227](#)].
- [28] J. Cogan, M. Kagan, E. Strauss and A. Schwartzman, *Jet-Images: Computer Vision Inspired Techniques for Jet Tagging*, *JHEP* **02** (2015) 118, [[1407.5675](#)].
- [29] ATLAS collaboration, *Identification of boosted, hadronically decaying W bosons and comparisons with ATLAS data taken at $\sqrt{s} = 8$ TeV*, *Eur. Phys. J. C* **76** (2016) 154, [[1510.05821](#)].
- [30] ATLAS collaboration, *A new method to distinguish hadronically decaying boosted Z bosons from W bosons using the ATLAS detector*, *Eur. Phys. J. C* **76** (2016) 238, [[1509.04939](#)].
- [31] K. Datta and A. Larkoski, *How Much Information is in a Jet?*, *JHEP* **06** (2017) 073, [[1704.08249](#)].
- [32] Y.-C. J. Chen, C.-W. Chiang, G. Cottin and D. Shih, *Boosted W and Z tagging with jet charge and deep learning*, *Phys. Rev. D* **101** (2020) 053001, [[1908.08256](#)].
- [33] X. Ju and B. Nachman, *Supervised Jet Clustering with Graph Neural Networks for Lorentz Boosted Bosons*, *Phys. Rev. D* **102** (2020) 075014, [[2008.06064](#)].
- [34] J. Lin, M. Freytsis, I. Moulton and B. Nachman, *Boosting $H \rightarrow b\bar{b}$ with Machine Learning*, *JHEP* **10** (2018) 101, [[1807.10768](#)].
- [35] ATLAS collaboration, *Identification of boosted Higgs bosons decaying into b-quark pairs with the ATLAS detector at 13 TeV*, *Eur. Phys. J. C* **79** (2019) 836, [[1906.11005](#)].

- [36] A. Chakraborty, S. H. Lim and M. M. Nojiri, *Interpretable deep learning for two-prong jet classification with jet spectra*, *JHEP* **19** (2020) 135, [[1904.02092](#)].
- [37] E. A. Moreno, T. Q. Nguyen, J.-R. Vlimant, O. Cerri, H. B. Newman, A. Periwai et al., *Interaction networks for the identification of boosted $H \rightarrow b\bar{b}$ decays*, *Phys. Rev. D* **102** (2020) 012010, [[1909.12285](#)].
- [38] A. Ali, F. Barreiro and T. Lagouri, *Prospects of measuring the CKM matrix element $|V_{ts}|$ at the LHC*, *Phys. Lett. B* **693** (2010) 44, [[1005.4647](#)].
- [39] J. Duarte-Campderros, G. Perez, M. Schlaffer and A. Soffer, *Probing the Higgs–strange-quark coupling at e^+e^- colliders using light-jet flavor tagging*, *Phys. Rev. D* **101** (2020) 115005, [[1811.09636](#)].
- [40] SLD collaboration, *Light quark fragmentation in polarized Z^0 decays at SLD*, *Nucl. Phys. B Proc. Suppl.* **96** (2001) 31, [[hep-ex/0008032](#)].
- [41] DELPHI collaboration, *Measurement of the strange quark forward-backward asymmetry around the Z^0 peak*, *Eur. Phys. J. C* **14** (2000) 613.
- [42] J. Erdmann, *A tagger for strange jets based on tracking information using long short-term memory*, *JINST* **15** (2020) P01021, [[1907.07505](#)].
- [43] Y. Nakai, D. Shih and S. Thomas, *Strange Jet Tagging*, [2003.09517](#).
- [44] L. de Oliveira, M. Kagan, L. Mackey, B. Nachman and A. Schwartzman, *Jet-images — deep learning edition*, *JHEP* **07** (2016) 069, [[1511.05190](#)].
- [45] D. Guest, J. Collado, P. Baldi, S.-C. Hsu, G. Urban and D. Whiteson, *Jet Flavor Classification in High-Energy Physics with Deep Neural Networks*, *Phys. Rev. D* **94** (2016) 112002, [[1607.08633](#)].
- [46] J. Aguilar-Saavedra, J. H. Collins and R. K. Mishra, *A generic anti-QCD jet tagger*, *JHEP* **11** (2017) 163, [[1709.01087](#)].
- [47] G. Louppe, K. Cho, C. Becot and K. Cranmer, *QCD-Aware Recursive Neural Networks for Jet Physics*, *JHEP* **01** (2019) 057, [[1702.00748](#)].
- [48] T. Heimel, G. Kasieczka, T. Plehn and J. M. Thompson, *QCD or What?*, *SciPost Phys.* **6** (2019) 030, [[1808.08979](#)].
- [49] P. T. Komiske, E. M. Metodiev, B. Nachman and M. D. Schwartz, *Learning to classify from impure samples with high-dimensional data*, *Phys. Rev. D* **98** (2018) 011502, [[1801.10158](#)].
- [50] D. Belayneh et al., *Calorimetry with deep learning: particle simulation and reconstruction for collider physics*, *Eur. Phys. J. C* **80** (2020) 688, [[1912.06794](#)].
- [51] E. A. Moreno, O. Cerri, J. M. Duarte, H. B. Newman, T. Q. Nguyen, A. Periwai et al., *JEDI-net: a jet identification algorithm based on interaction networks*, *Eur. Phys. J. C* **80** (2020) 58, [[1908.05318](#)].
- [52] H. Qu and L. Gouskos, *ParticleNet: Jet Tagging via Particle Clouds*, *Phys. Rev. D* **101** (2020) 056019, [[1902.08570](#)].
- [53] E. Bols, J. Kieseler, M. Verzetti, M. Stoye and A. Stakia, *Jet Flavour Classification Using DeepJet*, [2008.10519](#).
- [54] S. Hochreiter and J. Schmidhuber, *Long Short-Term Memory*, *Neural Comput.* **9** (1997) 1735.
- [55] J. Alwall, M. Herquet, F. Maltoni, O. Mattelaer and T. Stelzer, *MadGraph 5: going beyond*, *JHEP* **06** (2011) 128, [[1106.0522](#)].
- [56] R. D. Ball et al., *Parton distributions with LHC data*, *Nucl. Phys. B* **867** (2013) 244, [[1207.1303](#)].

- [57] T. Sjöstrand, S. Ask, J. R. Christiansen, R. Corke, N. Desai, P. Ilten et al., *An introduction to PYTHIA 8.2*, *Comput. Phys. Commun.* **191** (2015) 159, [[1410.3012](#)].
- [58] M. Cacciari, G. P. Salam and G. Soyez, *The anti- k_t jet clustering algorithm*, *JHEP* **04** (2008) 063, [[0802.1189](#)].
- [59] M. Cacciari, G. P. Salam and G. Soyez, *FastJet user manual*, *Eur. Phys. J. C* **72** (2012) 1896, [[1111.6097](#)].
- [60] M. Cacciari, G. P. Salam and G. Soyez, *The catchment area of jets*, *JHEP* **04** (2008) 005, [[0802.1188](#)].
- [61] CMS collaboration, *Measurement of charged pion, kaon, and proton production in proton-proton collisions at $\sqrt{s} = 13$ TeV*, *Phys. Rev. D* **96** (2017) 112003, [[1706.10194](#)].
- [62] F. Pedregosa et al., *Scikit-learn: Machine Learning in Python*, *J. Machine Learning Res.* **12** (2011) 2825, [[1201.0490](#)].
- [63] F. Chollet et al., “Keras.” <https://keras.io>, 2015.
- [64] M. Abadi et al., “TensorFlow: Large-scale machine learning on heterogeneous distributed systems.” <https://www.tensorflow.org>, 2015.
- [65] D. P. Kingma and J. Ba, *Adam: A Method for Stochastic Optimization*, [1412.6980](#).
- [66] J. de Favereau, C. Delaere, P. Demin, A. Giammanco, V. Lemaître, A. Mertens et al., *DELPHES 3: a modular framework for fast simulation of a generic collider experiment*, *JHEP* **02** (2014) 057, [[1307.6346](#)].